IEEE Access
Multidisciplinary | Rapid Review | Open Access Journal

Received January 14, 2020, accepted February 3, 2020, date of publication February 17, 2020, date of current version March 3, 2020.

Digital Object Identifier 10.1109/ACCESS.2020.2974321

Study on Optimal Laminographic Tilt Angle: A Method for Analyzing Quantity Information Gained in Projections

YIMING JIANG[1,2], JING ZOU[1,2], XIAODONG HU[1,2], ZHENYE HAN[1,2], YANTAO MU[1,2], MING CHEN[3], AND YING XU[4]

[1]State Key Laboratory of Precision Measuring Technology and Instruments, Tianjin University, Tianjin 300072, China
[2]Nanchang Institute for Micro Technology, Tianjin University, Tianjin 300072, China
[3]College of Mathematics and Systems Science, Shandong University of Science and Technology, Qingdao 266590, China
[4]School of Electromechanical Engineering, Guangdong University of Technology, Guangzhou 510006, China

Corresponding author: Jing Zou (jingzoutd@tju.edu.cn)

This work was supported in part by the National Natural Science Foundation of China under Grant 61771328, and in part by the National Key Research and Development Program of China under Grant 2017YFB1103900.

ABSTRACT In laminography imaging, the laminographic tilt angle is an important factor that affects the reconstruction result. However, the optimal tilt angle was mainly estimated from experience in the current research. In this article, an estimation approach for measuring the quantity information of projections has been proposed, which is based on the entropy of pixel grayscale distribution. The correlation of reconstructed image quality and tilt angle was analyzed quantitatively by the method. In this way, a solution has been proposed for seeking the optimal tilt angle, which aims to improve the image quality of reconstructed layers. Additionally, numerical simulation was designed to validate the method, in which the reconstructed layer images at different tilt angles were compared. The curves of grayscale MAE, PSNR and SSIM versus tilt angle verified the reliability of calculated optimal tilt angle, which has proved that the method is effective. Meanwhile, given a certain model of the scanned object, the optimal tilt angle is constant and computable.

INDEX TERMS Laminography, optimization, quantity information, image reconstruction, image quality, numerical simulation.

I. INTRODUCTION

Computed tomography (CT), as an efficient non-destructive testing method, is widely used in biomedical, industrial manufacturing, security and other fields. CT imaging relies on a decrease of the intensity (attenuation) of X-ray beam when traversing the sample, which can be measured directly with the assistance of an X-ray detector. The attenuation coefficient is determined by the property of penetrated medium. In the scanning process, the sample rotates around the fixed axis step by step in 360 degrees. Corresponding projection image is collected by the detector at each angle. After acquisition of projections from all angles, a reconstruction algorithm is used to obtain image data of sectional layers, then the three-dimensional internal structure of the object is visible by stacking the sectional images one by one.

The associate editor coordinating the review of this manuscript and approving it for publication was Zhenliang Zhang.

However, circular cone beam CT is not suitable for imaging of flat objects such as circuit boards, composite plates, etc. The X-ray penetration distance in a flat object changes obviously in different projection directions, which leads to the lack of projection image data at some angles. The problem of imaging flat objects has challenged the traditional CT technology, which has promoted the development of laminography. The earliest linear tomography device, which is also considered as the original laminography device, was proposed and designed by Andre Edmond Marie Bocage in 1921 [1], [2]. Later, Bernard Zeidses des Plantes verified the tomography method both theoretically and experimentally. The tomographic principle, originally called ''planography'', was presented in his doctoral thesis in 1931 [1], [2]. Based on the principle of classical tomography, the multiple-film laminography and relative reconstruction methods were proposed in the early 1970s [3], [4], and then it gradually developed into computed laminography (CL) in 1995 [5].

The planar laminography is the earliest experimental method. It was proved to be a superior way for imaging flat objects than CT [6], [7]. The appearance of swing laminography [8] and rotary laminography [9]–[11] symbolized the evolution of CL scanning method, which improved the projection data acquisition. Currently, the rotary laminography is commonly used in engineering and scientific experiments, and it has showed advantages in limited-angle imaging [12].

In view of the scanning geometries, the CL scan obtains more sufficient projection data than the traditional circular CT scan. That is the reason why CL is more suitable for imaging plate objects. In the same way, scanning geometries of CL have direct and obvious effects on data acquisition whose difference will ultimately be reflected in the reconstruction results. Some relevant experiments and corresponding summaries were made for specific samples [10], [13]. Accurate analysis of optimal scanning geometry has great significance for CL imaging. For the rotary laminography, the tilt angle is a key geometric factor. In this article, the influence of laminographic tilt angle on reconstruction results have been analyzed from the perspective of the difficulty of accurate reconstruction, which involves the maximum likelihood estimation whose constraints are provided by projection images. The optimal tilt angle maximizes the probability of accurate reconstruction under projection constraints. On the other hand, a simulation experiment is needed to validate the optimization method. In our simulation, the laminographic tilt angle was adjusted by changing the X-ray projection directions. Based on the projection images, SART (simultaneous algebraic reconstruction technique) algorithm was used to reconstruct the object. In order to precisely measure the accuracy of reconstructions at different tilt angles, the grayscale MAE (mean absolute error), PSNR (peak signal to noise ratio) and SSIM (structural similarity index) were used as quantitative indicators. The reconstructed image that is closer to the original version has higher image quality, which results in higher PSNR, SSIM value and lower MAE. The curves of three indicators changing with tilt angle show that the experimental optimal tilt angle matches the calculated result. Therefore, the method has been proved to be useful for optimizing laminographic tilt angle.

II. ESSENTIAL FACTORS FOR RECONSTRUCTION

A. BEER-LAMBERT LAW

The basic principle of CT reconstruction is to distinguish substances according to the change of X-ray attenuation degree in different directions. According to Beer-Lambert law,

$$I_L = I_{L0}\exp\left(-g_L\right), \tag{1.1}$$

where I_{L0} represents the initial X-ray intensity along L; I_L represents X-ray intensity after penetrating the object; g_L is the complete projection along L,

$$g_L = \int_0^l \mu\left(x, y\right) dL, \tag{1.2}$$

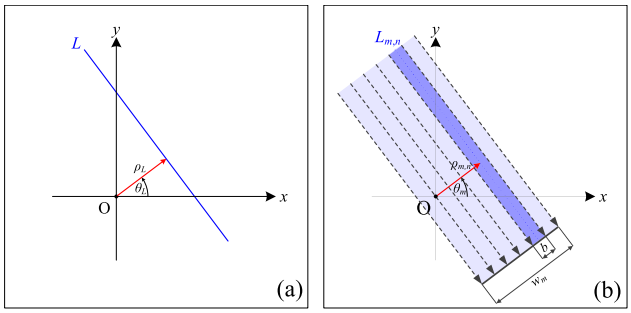

FIGURE 1. Diagram of Radon transforms: (a) projection along straight line L; (b) projections along the same direction in B_m.

where l indicates the length of X-ray transmission in the object; $\mu\left(x, y\right)$ represents the attenuation coefficient of the substance at the (x, y) position.

B. RADON TRANSFORM

The Radon transform is an integral transform, which maps the line integral of the function defined on the x-y plane to the value of a point on the projection plane [14], [15]. According to the normal form equation of L,

$$L : x\cos\theta_L + y\sin\theta_L = \rho_L, \tag{1.3}$$

where the normal vector from origin O to L has length ρ_L. It subtends an angle θ_L with the positive direction of x-axis. θ_L is defined as the projection angle. L on the x-y plane corresponds to (ρ_L, θ_L) on the projection plane. The diagram is shown in Fig.1-(a). The complete projection g_L on the coordinate (ρ_L, θ_L) are given by the integral of the attenuation coefficient along L, which is

$$\begin{aligned} g_L &= \int_{-\infty}^{\infty}\int_{-\infty}^{\infty} \mu\left(x, y\right)\delta\left(x\cos\theta_L + y\sin\theta_L - \rho_L\right) dxdy \\ &= \int_{-\infty}^{\infty} \mu((l\sin\theta_L + \rho_L\cos\theta_L), (-l\cos\theta_L + \rho_L\sin\theta_L))dl, \end{aligned} \tag{1.4}$$

where

$$\delta\left(t\right) = \begin{cases} 1, & t = 0 \\ 0, & t \neq 0, \end{cases} \tag{1.5}$$

For the circular CT scan, suppose there exists multiple parallel X-ray projection beams in two-dimensional plane. The projection beams are marked by $\{B_m\}\,(m = 1, 2, \ldots, M)$. The B_m represents a series of projection line at the m-th projection angle θ_m, whose width w_m is equal to that of the object in the same direction. $L_{m,n}\,(n = 1, 2, \ldots, N_m)$ is the n-th projection line in B_m. $L_{m,n}$ has fixed width b, and

$$w_m = bN_m, \tag{1.6}$$

The projection $g_{m,n}$ of $L_{m,n}$ is the integral of line projection along the normal direction of $L_{m,n}$. If the central axis of $L_{m,n}$

is represented on the projection plane as $(\rho_{m,n}, \theta_m)$, which is shown in Fig.1-(b), then

$$g_{m,n} = \int_{\rho_{m,n}-\frac{1}{2}b}^{\rho_{m,n}+\frac{1}{2}b} g_L(\rho, \theta_m)\, d\rho = \int_{-\infty}^{\infty}\int_{-\infty}^{\infty} \mu(x, y)\, \delta_{m,n}(x, y)\, dxdy, \quad (1.7)$$

where,

$$\delta_{m,n}(x, y) = \begin{cases} 1, & |x \sin\theta_m + y\cos\theta_m - d_{m,n}| \le \frac{b}{2} \\ 0, & |x \sin\theta_m + y\cos\theta_m - d_{m,n}| > \frac{b}{2}. \end{cases} \quad (1.8)$$

Consider that $\mu(x, y)$ has positive value only in a limited region $R(\mu)$, which is the solution domain of $\mu(x, y)$. $R(\mu)$ is composed of discrete pixels (square shaped) marked as $\{p_i\}$ $(i = 1, 2, \ldots, N)$. By taking the mean of the integral of $\mu(x, y)$ in the p_i area, $\mu(x, y)$ is discretized as μ_i,

$$\mu_i = a^{-2} \iint_{p_i} \mu(x, y)\, dxdy. \quad (1.9)$$

μ_i is assumed to be constant in the i-th pixel p_i. a is the size (side length) of each pixel. Then

$$g_{m,n} = a^2 \sum_{i=1}^{N} \mu_i \delta_{m,n}(i). \quad (1.10)$$

where μ_i is the X-ray attenuation coefficient in the i-th pixel p_i; $\delta_{m,n}(i)$ is defined by

$$\delta_{m,n}(i) = a^{-2} \iint_{p_i} \delta_{m,n}(x, y)\, dxdy. \quad (1.11)$$

If $N \to \infty$, μ_i can infinitely approach continuous distribution of $\mu(x, y)$.

III. QUANTITY INFORMATION OF PROJECTION IMAGES

X-ray projection is essentially a mapping of pixels from three-dimensional space to two dimensional plane. Obviously, the projection forms a continuous function. The X-ray projection is a multitude-to-one mapping from the object to the detector. That is to say, the projection image is the superposition result of X-ray attenuation images on multiple layers. Projections act as the carrier of information, for each of them can partly reflect the internal structure of the object.

If the image to be reconstructed is regarded as a system with arbitrary distribution of μ_i in the solution domain $R(\mu)$ which is the common area covered by all projections, then each projection is a constraint on μ_i distribution which reduces the set of possible solutions for μ_i distribution. Without any projection information as the constraint, the distribution of μ_i has great uncertainty. Referring to Maxwell's demon theory, the internal energy of a system tends to be uniform and chaotic when there is no external information input [16]. The accumulated projection information is equivalent to the input of certain external energy to the reconstruction region, which makes the inner part of the reconstruction region orderly. That is a process of entropy reduction. If we take the number of possible μ_i distributions as the μ_i entropy, then the quantity information of X-ray projections can be evaluated by the reduction of entropy, which is introduced by projections.

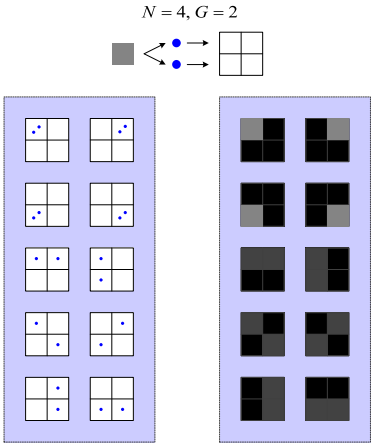

FIGURE 2. Example: The possible distributions of $G = 2$ particles in $N = 4$ pixels, where each particle represents a certain value of attenuation coefficient and image gray-level.

A. ANALYSIS OF RECONSTRUCTION COMPLEXITY

For a CT image to be reconstructed, assume the solution domain $R(\mu)$ is divided into total N pixels. $\overline{\mu}$ is the average attenuation coefficient of the total pixels,

$$\overline{\mu} = \frac{1}{N} \sum_{i=1}^{N} \mu_i. \quad (2.1)$$

$\overline{\mu} > 0$. The reconstruction process can be regarded as distributing the μ_i value (where $i = 1, 2, \ldots, N$) into image pixels. The minimum μ_i of each pixel is 0. If the area of the reconstructed region $R(\mu)$ is A_R, and the pixel size is a, then

$$N = a^{-2} A_R. \quad (2.2)$$

In order to quantify all possible solutions of μ_i distribution, we consider every μ_i to be composed of the minimum $\Delta\mu$ that cannot be subdivided, where $\frac{\Delta\mu}{\overline{\mu}} \to 0$. The process refers to the principle of energy dispersion in quantum mechanics. Then the sum of μ_i is discretized into G particles of $\Delta\mu$. The problem is transformed into how many possibilities for plugging total G particles into N pixels. For example, if a total of 2 particles are randomly plugged into 4 pixels ($G = 2$, $N = 4$), there will be 10 cases, which is shown in Fig.2.

Combined with (2.1), G satisfies

$$G = \frac{1}{\Delta\mu} \sum_{i=1}^{N} \mu_i = \eta \overline{\mu} N, \quad (2.3)$$

where η is the resolution of μ_i value, $\eta = \frac{1}{\Delta\mu}$, $\eta\overline{\mu} \to \infty$. If $N_s \big|_G^{\mu}$ is the total quantity of solutions for the possible

distribution of attenuation coefficient μ_i with total G particles in the image, then

$$N_s\left|_G^{\mu}\right. = C_T^{N-1} = \frac{\Gamma(T+1)}{\Gamma(N)\cdot\Gamma(G+1)}. \tag{2.4}$$

where, C_T^{N-1} is for the combination of $N-1$ elements from T elements, $T = N+G-1$; the gamma function for integer $Z \geq 0$ is

$$\Gamma(Z+1) = \int_0^{\infty} t^Z e^{-t} dt = Z!, \tag{2.5}$$

the symbol $N_s\left|_{\psi}^{\phi}\right.$ denotes the quantity of solutions for ϕ under the constraint ψ. The larger the $N_s\left|_G^{\mu}\right.$, the more conditions are required for accurate reconstruction.

By Stirling's approximation [17],

$$\Gamma(Z+1) \approx \sqrt{2\pi Z}\left(\frac{Z}{e}\right)^Z. \tag{2.6}$$

Substitute formula (2.6) into (2.4),

$$N_s\left|_G^{\mu}\right. \approx \frac{1}{\sqrt{2\pi}}\sqrt{\frac{1}{N-1}+\frac{1}{G}}\cdot\frac{T^T}{(N-1)^{N-1}G^G}. \tag{2.7}$$

Considering the situation $N = 1$ or $G = 0$, such approximation is used instead of (2.7), as

$$N_s\left|_G^{\mu}\right. \approx \sqrt{\frac{1}{1+2\pi(N-1)}+\frac{1}{1+2\pi G}}\cdot\frac{T^T}{(N-1)^{N-1}G^G}. \tag{2.8}$$

Substitute formula (2.3) into (2.8), then (2.8) equals to

$$N_s\left|_G^{\mu}\right. \approx \sqrt{\frac{1}{1+2\pi(N-1)}+\frac{1}{1+2\pi\eta\overline{\mu}N}}\cdot\left(1+\frac{\eta\overline{\mu}N}{N-1}\right)^{N-1}\left(1+\frac{N-1}{\eta\overline{\mu}N}\right)^{\eta\overline{\mu}N}. \tag{2.9}$$

Consider that $\eta\overline{\mu} \to \infty$, $N \gg 1$, by further approximation,

$$N_s\left|_G^{\mu}\right. \approx \frac{(\eta\overline{\mu})^{N-1}\exp(N)}{\sqrt{1+2\pi N}}. \tag{2.10}$$

We take any of these possible solutions as the reconstruction result, if event $\mu_i \sim \mu$ represents the solution for μ_i happens to subject the accurate attenuation coefficient distribution of real image, then the probability $P(\mu|G)$ is

$$P(\mu|G) = \left(N_s\left|_G^{\mu}\right.\right)^{-1}. \tag{2.11}$$

Obviously, there is an increased difficulty for reconstruction with smaller $P(\mu|G)$. The entropy of μ_i distribution in reconstructed region is defined as $S(\mu)$,

$$S(\mu) = \ln\left(N_s\left|_G^{\mu}\right.\right) = -\ln P(\mu|G). \tag{2.12}$$

Substitute (2.2), (2.10) and (2.11) into (2.12),

$$S(\mu) = (N-1)\ln(\eta\overline{\mu}) + N - \frac{1}{2}\ln(1+2\pi N). \tag{2.13}$$

The conditions required for solving the μ_i distribution is

$$N_{\text{con}}(\mu) = \lim_{\eta\overline{\mu}\to\infty}\frac{S(\mu)}{\ln(\eta\overline{\mu})} = N-1. \tag{2.14}$$

Formula (2.14) shows that $N_{\text{con}}(\mu)$ is almost equal to the total pixel quantity N, which is approximately proportional to the reconstructed area A_R and inversely proportional to the pixel area a^2 according to (2.2).

B. QUANTITY INFORMATION OF SINGLE PROJECTION IMAGE

The entropy of μ_i distribution in reconstructed region has been quantified in the former section. A single projection reflects some internal details of the object, which reduces the entropy of the reconstructed region. Generally, the quantity information obtained by the projection in a certain direction depends on the quantity of projection lines. Accordingly, the projection image reflects more information with shorter X-ray crossing length through the object. For an object with negligible thickness, a single X-ray projection along the thickness direction can completely reflect the whole inner material distribution.

Through the analysis in the former section, we have deduced the conclusion that if a random solution of μ_i distribution approaches the real μ distribution, the probability is inversely proportional to the quantity of total solutions for μ_i distribution. In order to increase the probability of accurate reconstruction, we introduce a constraint ψ for the image. The quantity of solutions under ψ is $N_s\left|_{\psi}^{\mu}\right.$, $N_s\left|_{\psi}^{\mu}\right. \leq N_s\left|_G^{\mu}\right.$. The probability of accurate reconstruction under constraint ψ is

$$P(\mu|\psi) = \left(N_s\left|_{\psi}^{\mu}\right.\right)^{-1}, \tag{2.15}$$

where $P(\mu|\psi)$ is the conditional probability under constraint ψ. Furthermore, the probability that any solution for μ_i that satisfies constraint ψ is

$$P(\psi|G) = P(\mu|G)\cdot P^{-1}(\mu|\psi) = \left(N_s\left|_G^{\mu}\right.\right)^{-1}\cdot\left(N_s\left|_{\psi}^{\mu}\right.\right), \tag{2.16}$$

where $P(\psi|G)$ is the probability that a random solution for μ satisfies ψ. If $S(\psi)$ is the entropy of ψ, then $Q(\psi)$ is defined as

$$S(\psi) = -\ln P(\psi|G) = S(\mu) - S(\mu|\psi). \tag{2.17}$$

where $S(\mu|\psi)$ is the entropy of μ_i distribution under constraint ψ, and $S(\mu|\psi) = \ln\left(N_s\left|_{\psi}^{\mu}\right.\right)$.

If $P(\psi|G) \to P(\mu|G)$, then $S(\psi) \to S(\mu)$, the solution for μ_i under ψ tends to be unique. As a result, the information provided by constraint ψ is enough to accurately reconstruct the image.

Take the grayscale distribution of projection beam B_m as the constraint ψ. For the projection beam B_m within $R(\mu)$, it divides the images into N_m parts,

$$N_m = b^{-1}w_m, \tag{2.18}$$

where b is the width of each projection line $L_{m,n}$, w_m is the width of B_m. Within the projection line $L_{m,n}$,

$$N_{m,n} = a^{-2} b l_{m,n}, \tag{2.19}$$

where $l_{m,n}$ is the length of each projection line $L_{m,n}$ through $R(\mu)$. Given the constraint that $L_{m,n}$ has $G_{m,n}$ particles of $\Delta\mu$ and $N_{m,n}$ pixels, as

$$G_{m,n} = \eta \overline{\mu}_{m,n} N_{m,n}, \tag{2.20}$$

where $\overline{\mu}_{m,n}$ is the average attenuation coefficient in $L_{m,n}$, and $\overline{\mu}_{m,n} > 0$. The quantity of possible solutions is

$$N_s \left|_{B_m}^{\mu} \right. = \prod_{n=1}^{N_m} C_{T_{m,n}}^{N_{m,n}-1}. \tag{2.21}$$

By further approximation,

$$N_s \left|_{B_m}^{\mu} \right. = \left(\prod_{n=1}^{N_m} \frac{(\eta \overline{\mu}_{m,n})^{N_{m,n}-1}}{\sqrt{1 + 2\pi N_{m,n}}} \right) \exp(N). \tag{2.22}$$

And also

$$N_s \left|_{B_m}^{\mu} \right. \leq \frac{(\eta \overline{\mu})^{N-N_m} \exp(N)}{\prod_{n=1}^{N_m} \sqrt{1 + 2\pi N_{m,n}}}. \tag{2.23}$$

Only when $\overline{\mu}_{m,n} = \frac{(N_{m,n}-1)N}{(N-N_m)N_{m,n}} \overline{\mu} \approx \overline{\mu}$, formula (2.23) takes the maximum. According to (2.16), given the constraint $\psi|B_m\rangle$ that each projection line $L_{m,n}$ has $G_{m,n}$ particles of $\Delta\mu$, the probability that a random solution for μ_i with total G particles satisfies the constraint $\psi|B_m\rangle$ is

$$\begin{aligned} P(B_m|G) &= \left(N_s \left|_{G}^{\mu}\right.\right)^{-1} \cdot \left(N_s \left|_{B_m}^{\mu}\right.\right) \\ &\leq \frac{\sqrt{1 + 2\pi N}}{\prod_{n=1}^{N_m} \left(\sqrt{1 + 2\pi N_{m,n}}\right)} (\eta \overline{\mu})^{-(N_m - 1)}. \end{aligned} \tag{2.24}$$

Consider that $S(B_m)$ is affected by the distribution of μ_i, we use the $S_{\min}(B_m)$ to estimate the entropy of B_m, which is

$$\begin{aligned} S_{\min}(B_m) \approx (N_m - 1) \ln(\eta \overline{\mu}) + \frac{1}{2} \ln(1 + 2\pi N) \\ - \frac{1}{2} \sum_{n=1}^{N_m} \ln\left(1 + 2\pi N_{m,n}\right). \end{aligned} \tag{2.25}$$

By referring to (2.14), we obtain the relation

$$N_{\text{con}}(B_m) = \lim_{\eta\overline{\mu} \to \infty} \frac{S_{\min}(B_m)}{\ln(\eta \overline{\mu})} = N_m - 1, \tag{2.26}$$

where $N_{\text{con}}(B_m)$ is the condition number of B_m, which means the projection B_m reduces at least $N_{\text{con}}(B_m)$ conditions for image reconstruction.

According to (2.17),

$$S_{\max}(\mu|B_m) = S(\mu) - S_{\min}(B_m). \tag{2.27}$$

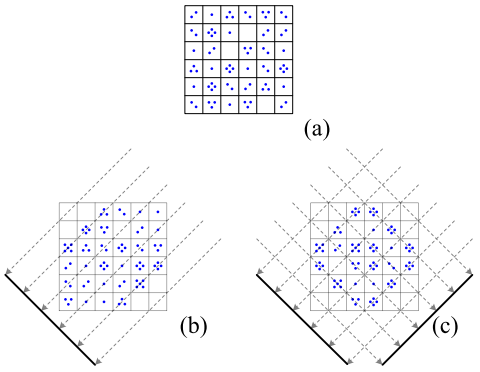

FIGURE 3. Diagram: The μ_i distribution of ($N = 36$, $G = 72$) tends to be orderly under the constraints of projections. (a) random particle distribution; (b) particle distribution that satisfies the constraint of a single projection; (c) particle distribution that satisfies the constraint of two orthogonal projections.

Substitute (2.14) and (2.26) into (2.27), we get

$$P(\mu|B_m) \geq \exp(-S_{\max}(\mu|B_m)) \approx (\eta \overline{\mu})^{N_m - N}, \tag{2.28}$$

where $P(\mu|B_m)$ is the probability of obtaining accurate μ_i distribution under constraint $\psi|B_m\rangle$. Formula (2.28) shows that larger condition number of B_m facilitates image reconstruction. $P(\mu|B_m)$ has an exponential correlation with $N_{\text{con}}(B_m)$.

The analysis indicates that projections carry a certain quantity of information into the solution domain $R(\mu)$. The quantity information can be presented by the condition number of each projection. The conditions provided by the projection images reduce the uncertainty of the solution in the reconstructed region. Therefore, the entropy of the system is reduced. The set of possible solutions shrinks gradually with the accumulation of projections in different directions. The principle can be intuitively reflected in Fig.3.

C. RECONSTRUCTIVE PRECISION OF PROJECTION GROUP

The entropy of every single projection B_m affects the data acquisition of X-ray scanning. Another factor is the similarity of projection images obtained from X-ray projection group $\{B_m\}$. If the projection directions have reduced intersected angles, the projection images have increased similarity. And larger similarity of projection images causes the quality of the reconstructed images to deteriorate.

The following parameters are known for group $\{B_m\}$: N_m is the quantity of projection lines in each B_m, M is the total number of projections, $\Delta\theta$ is the sampling interval angle. If $M > 1$, then total condition number of $\{B_m\}$ is

$$N_{\text{con}}\{B_m\} = \begin{cases} \sum_{m=1}^{M} N_m - \frac{M}{2} \cot\frac{\Delta\theta}{2} - 1, N_m \geq \cot\frac{\Delta\theta}{2} \\ \frac{1}{2} \sum_{m=1}^{M} N_m^2 \tan\frac{\Delta\theta}{2} - 1, N_m < \cot\frac{\Delta\theta}{2}. \end{cases} \tag{2.29}$$

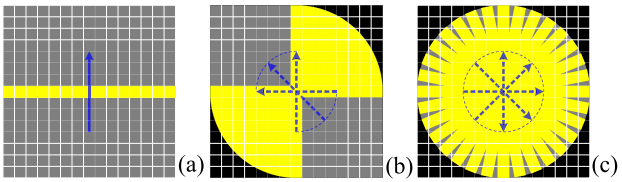

FIGURE 4. The relations among $A_{\text{con}}\{B_m\}$ (yellow colored region), $A_R\{B_m\}$ (gray and yellow colored region) and distribution of projections (M = 16): (a) projections overlapping (b) projections in limited angle 90°; (c) projections equally spaced among circumference.

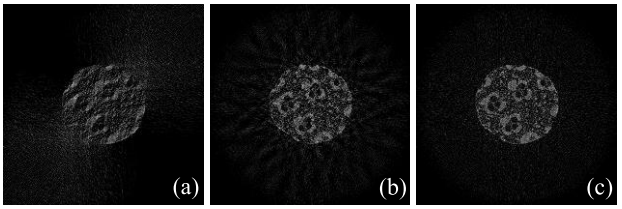

FIGURE 5. The reconstructed images of bamboo slice using equal numbers of projections with different distributions: (a) projections in limited angle 90°; (b) projections in nonadjacent 15° angles of equal interval 15°; (c) projections equally spaced.

The area of solvable domain related to $N_{\text{con}}\{B_m\}$ is

$$A_{\text{con}}\{B_m\} = b^2\left(1 + N_{\text{con}}\{B_m\}\right), \tag{2.30}$$

where b is the width of projection lines. In particular, if

$$N_{\text{con}}\{B_m\} = N_{\text{con}}(\mu) = N - 1, \tag{2.31}$$

then the image has enough conditions to be accurately reconstructed. Otherwise, the probability of the image being accurately reconstructed under $\psi\,|\{B_m\}\rangle$ satisfies

$$P(\mu\,|\{B_m\}) \geq (\eta\overline{\mu})^{N_{\text{con}}\{B_m\}-N}. \tag{2.32}$$

Consider that the attenuation coefficients of all pixels covered by zero-value projection lines are all zero. The solution domain $R(\mu)$ is regarded as the common area covered by $\{B_m\}$. For the image with pixel size a which can be accurately reconstructed by $\{B_m\}$, a must satisfy

$$a \geq a_{\min}\Big|^{\mu}_{\{B_m\}} = b\sqrt{\frac{A_R\{B_m\}}{A_{\text{con}}\{B_m\}}}, \tag{2.33}$$

where $A_R\{B_m\}$ is the area of solution domain.

Smaller pixel size leads to higher image resolution. Therefore, $a_{\min}\Big|^{\mu}_{\{B_m\}}$ reflects the reconstructive precision. It is determined by $A_{\text{con}}\{B_m\}$ and $A_R\{B_m\}$, affected by the distribution of $\{B_m\}$. An example is showed in Fig.4.

As a consequence, the reconstructive precision of circular projections is higher than that of limited-angle projections on the premise of equal projection numbers, showed in Fig.5. The main reason lies in that there are decreased condition number of projection group and increased solution domain area under limited-angle projections, which is not conducive to the pixel refining of accurate reconstruction. A reconstruction experiment for a bamboo stick fully has proved this fact. The reconstruction was performed with 360 projections extracted from 720 total circumferential projections of the bamboo stick sample.

On the premise of the same sampling number, the distribution of projections will significantly affect the acquired quantity information and the reconstruction results. The reconstructed image with equispaced projections, which corresponds to the minimum solution domain, has higher detail resolution than other cases. For the limited angle projections, the reconstructed image quality gradually improves as the projections tends to be uniformly distributed.

IV. OPTIMAL TILT ANGLE FOR FLAT OBJECTS

From the analysis in the former section, we estimated the reconstructive precision by the minimum pixel size of the image that can be accurately reconstructed. The quantity information of projection group is closely related to the reconstructive precision. In the laminographic scan, group $\{B_m(\varphi)\}$ represents the intersected parallel beam projections at tilt angle $\varphi(0 \leq \varphi \leq \frac{\pi}{2})$. The tilt angle is the included angle between the projection direction and the rotation axis. b is the size (side length) of square shaped cross-sectional area of each projection line. Assume the solution domain covered by $\{B_m(\varphi)\}$ has volume $V_R\{B_m(\varphi)\}$, then for the laminographic accurate reconstruction, the minimum voxel size is

$$a_{\min}\Big|^{\mu}_{\{B_m(\varphi)\}} = \sqrt[3]{\frac{V_R\{B_m(\varphi)\}}{1 + N_{\text{con}}\{B_m(\varphi)\}}} = b\sqrt[3]{\frac{V_R\{B_m(\varphi)\}}{V_{\text{con}}\{B_m(\varphi)\}}}, \tag{3.1}$$

in which

$$N_{\text{con}}\{B_m(\varphi)\} = b^{-3}V_{\text{con}}\{B_m(\varphi)\} - 1. \tag{3.2}$$

where $V_{\text{con}}\{B_m(\varphi)\}$ is the volume of solvable domain. The optimal laminographic tilt angle $\hat{\varphi}$ is acquired by

$$\hat{\varphi} = \arg\min_{\varphi}\left(a_{\min}\Big|^{\mu}_{\{B_m(\varphi)\}}\right) = \arg\min_{\varphi}\left(\frac{V_R\{B_m(\varphi)\}}{V_{\text{con}}\{B_m(\varphi)\}}\right). \tag{3.3}$$

In order to accurately describe the effect of the tilt angle on reconstructed image quality, we take a regular shaped object as an example. The method above can be used to find the optimal tilt angle for scanning a cylindrical object with radius r_0 and height h_0. The rotational axis passes through the center of round surfaces vertically. In the case of parallel projections, the X-ray beam passes through the object obliquely at tilt angle φ.

By geometric relations and some calculation, the volume of solvable domain is

$$V_{\text{con}}\{B_m(\varphi)\} = \frac{4}{3}\pi r_0^3 \sin\varphi\cos\varphi + \pi r_0^2 h_0 \sin^2\varphi. \tag{3.4}$$

And the volume of solution domain is

$$V_R\{B_m(\varphi)\} = \frac{2}{3}\pi r_0^3 \cot\varphi + \pi r_0^2 h_0. \tag{3.5}$$

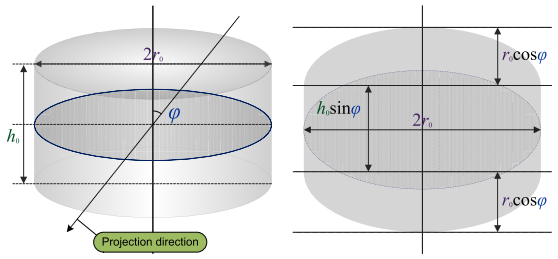

FIGURE 6. The cylindrical object model and its projection contour at tilt angle φ.

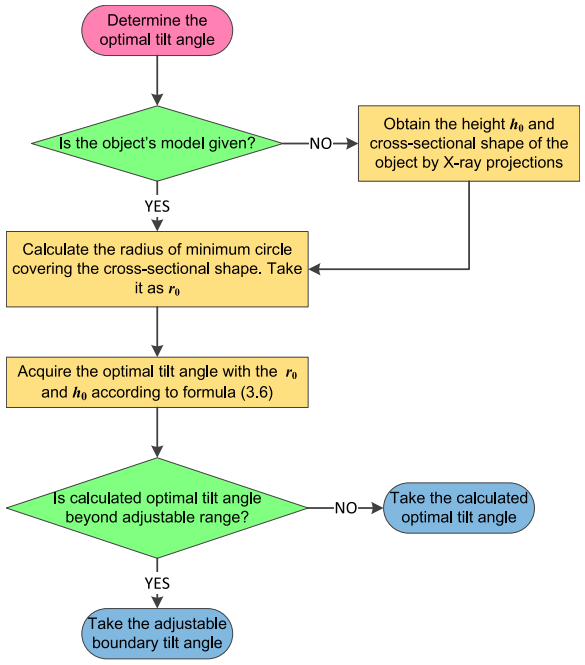

FIGURE 7. The flowchart of seeking the optimal laminographic tilt angle for an object with equal cross-sections.

According to formula (3.3), the optimal laminographic tilt angle $\hat{\varphi}$ is acquired by

$$\hat{\varphi} = \arg\min_{\varphi} \left(\frac{2\cot\varphi + 3r_0^{-1}h_0}{4\sin\varphi\cos\varphi + 3r_0^{-1}h_0\sin^2\varphi} \right). \quad (3.6)$$

$\hat{\varphi}$ depends on the size of r_0 and h_0 of the cylindrical object, which means the shape of the object may affect the relative quality of reconstructed images at a certain tilt angle. The object tends to be more 'flat' with decreased height-radius ratio $\frac{h_0}{r_0}$. Through the curve of $\frac{V_R}{V_{\text{con}}}$ versus φ, we can estimate the optimal tilt angle $\hat{\varphi}$ for cylindrical flat objects.

For a random shaped object with equal cross-sections, we use the cylinder model to estimate its optimal tilt angle for laminography. The flowchart of the proposed method is shown in Fig.7. The method is quite suitable for objects with equal convex polygon cross-sections, such as cuboids and hexagonal prisms which are common shapes of flat objects.

Furthermore, the method is also suitable for determining which placing attitude of the object is more conducive for CT

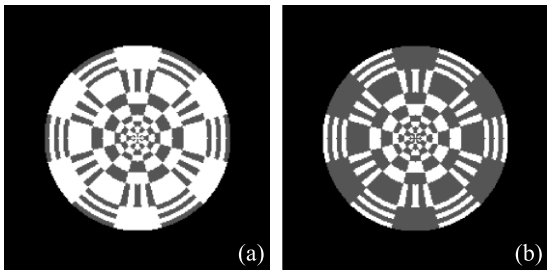

FIGURE 8. Original images of layers patterns: (a) pattern of even layers; (b) pattern of odd layers.

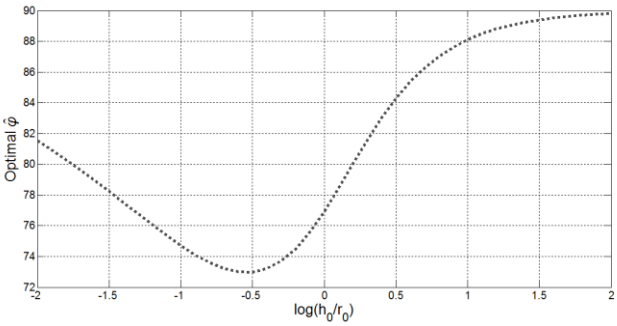

FIGURE 9. The relation curve of the predicted optimal tilt angle $\hat{\varphi}$ and the logarithm of ratio $\frac{h_0}{r_0}$ of cylindrical objects.

imaging. For imaging an IC chip as an example, it is better to place it vertically than lying down to acquire desirable reconstruction result, which can be well explained by this theory.

V. SIMULATION OF LAMINOGRAPHY SCAN AND RECONSTRUCTION

Some studies have shown that tilt angle can significantly influence the quality of reconstructed laminography images. The selection of optimal tilt angle is affected by both the object and sampling method [10], [18]. For the cylindrical object showed in Fig.6, a laminography imaging simulation was designed to verify the proposed method. As the experimental model, the cylinder is composed of two kinds of layers stacked alternately, whose patterns are showed by Fig.8. It was scanned by circular laminography of parallel projections with changeable tilt angle under simulated environment. The patterns inside the model depends on which layer they are located in. The sharpness of patterns of the reconstructed layer images reflects the quality of reconstruction.

According to formula (3.6), the relation of the estimated optimal tilt angle $\hat{\varphi}$ and the ratio $\frac{h_0}{r_0}$ of the cylindrical model can be calculated, shown in Fig.9. The relation illustrates that the optimal tilt angle varies from 73° to 90°.

In the first simulation, the height-radius ratio of the simulated object was set to $\frac{h_0}{r_0} = \frac{1}{80}$. The projections was made along changeable tilt angles, as $\varphi = (30°, 45°, 60°, 65°, 70°, 75°, 80°, 85°, 90°)$. The model was reconstructed by SART algorithm in the phantom. By observing the pattern image in each layer we can view the disparity of reconstructed images intuitively. Fig.10 shows the reconstructed images of the 254th layer. Visually, as the tilt angle

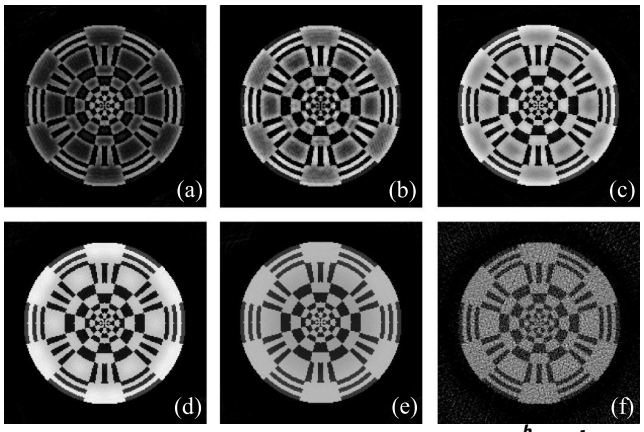

FIGURE 10. The reconstructed images of the 254th layer of $\frac{h_0}{r_0} = \frac{1}{80}$ at different tilt angles: (a) 45°; (b) 60°; (c) 70°; (d) 80°; (e) 85°; (f) 90°.

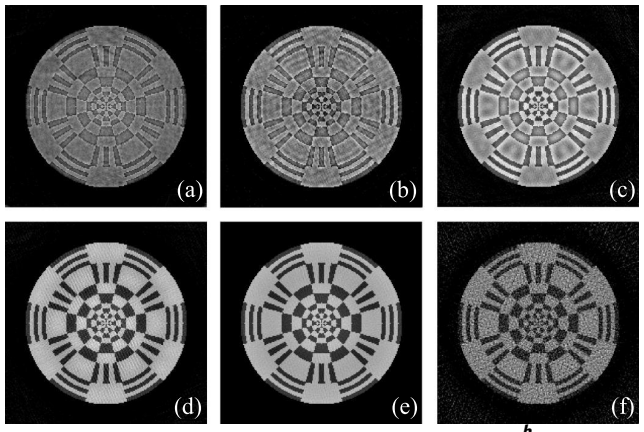

FIGURE 11. The reconstructed images of the 254th layer of $\frac{h_0}{r_0} = 6$ at different tilt angles: (a) 45°; (b) 60°; (c) 70°; (d) 80°; (e) 85°; (f) 90°.

increases, the image quality improves first and then deteriorates after a certain angle. Both the reconstructed layers at tilt angle 45° and 90° have relative degraded images, but not for the same reason. When the tilt angle is quite small, the main factor affecting image quality is the unevenly distribution of gray values, which is caused by the much larger solution domain than the actual region occupied by the object. And when the tilt angle is close to 90°, the low image quality is caused by the insufficient conditions provided by projections.

In the second simulation, the height-radius ratio of the simulated object was set to $\frac{h_0}{r_0} = 6$. Any other conditions were all same as those in the first simulation. Fig.11 shows the reconstructed images of the 254th layer. Compared with Fig.10, each reconstructed layer at tilt angle below 85° has reduced image quality. However, the reconstructed layer image at tilt angle 90° is exactly the same as that in Fig.9, which verifies that the proportion of the scanned object does not have an effect on CT imaging. Due to the change of the model shape, the optimal tilt angle is more close to 90°.

A. GRAYSCALE ABSOLUTE ERROR OF RECONSTRUCTED IMAGES

The proximity of reconstructed layer image to the original layer image is reflected by the grayscale absolute error. The

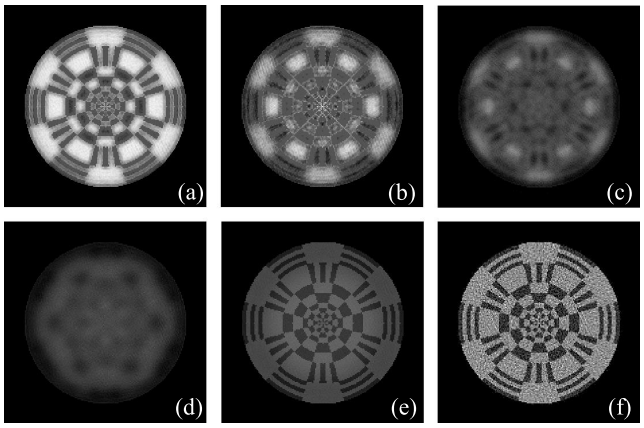

FIGURE 12. The grayscale absolute error images of 254th layer of $\frac{h_0}{r_0} = \frac{1}{80}$ at tilt angles: (a) 45°; (b) 60°; (c) 70°; (d) 80°; (e) 85°; (f) 90°.

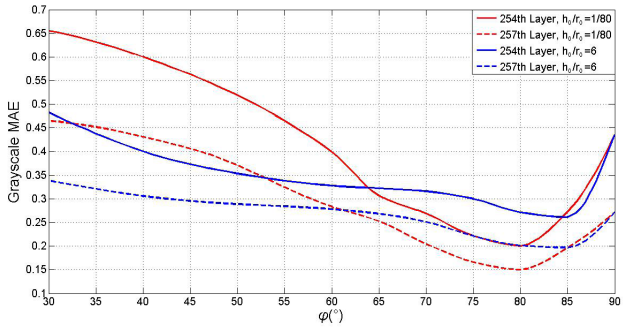

FIGURE 13. The φ-depended grayscale MAE curve of the 254th layer and the 257th layer.

grayscale difference image of the 254th layer ($\frac{h_0}{r_0} = \frac{1}{80}$), shown in Fig.12, directly reveals the accuracy of reconstruction.

Furthermore, the grayscale mean absolute error (MAE) of each pixel in the pattern image is calculated. It is indicated by the ratio of the actual grayscale error to the maximum pixel grayscale value. The grayscale MAE ranges from 0 to 1, where MAE = 0 means no error and MAE = 1 means the maximum limit error. The curve of grayscale MAE versus tilt angle is shown in Fig.13. Better image reconstruction accuracy will lead to a reduction in MAE. It can be observed from Fig.13 that the grayscale MAE decreases first and then increases after a certain tilt angle, which confirms the visual conclusion. In the second simulation, the minimum MAE point is closer to 90° in the x-axis compared to that in the first simulation. Fig.13 also shows the similarity of MAE curve shapes of different layers in the same model.

B. IMAGE QUALITY EVALUATED BY PSNR AND SSIM

In order to objectively evaluate the quality of reconstructed images, PSNR and SSIM were used to evaluate the quality of reconstructed images at specific layers. PSNR, short for peak signal to noise ratio, is a pixel-wise error metric, which is normally used to judge CT image quality based MSE measure [19], [20]. SSIM, short for structural similarity index, is regarded as a robust measure to compare image quality for CT reconstructions relative to a reference [21], [22]. By comparing with the original images in the phantom, the PSNR and

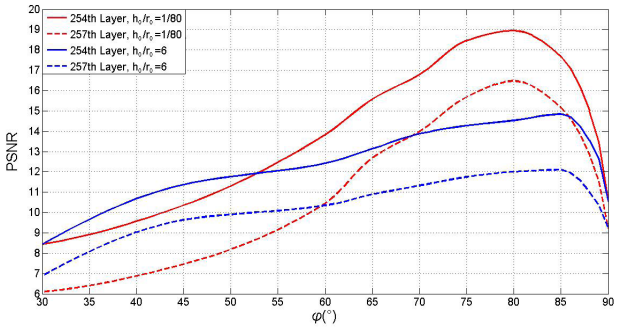

FIGURE 14. The φ-depended image PSNR curve of the 254th layer and the 257th layer.

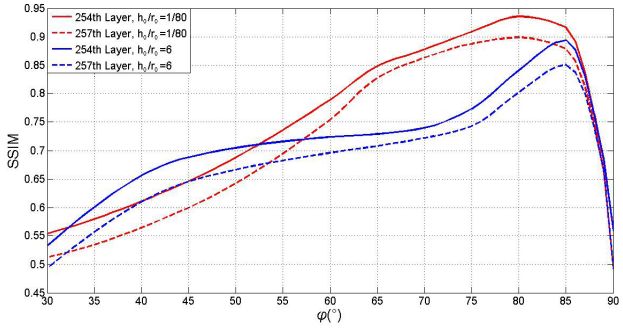

FIGURE 15. The φ-depended image SSIM curve of the 254th layer and the 257th layer.

SSIM values of 254th layer image and 257th layer image at each sampling tilt angle were calculated and fitted in continuous curves. The PSNR curve is shown in Fig.14 and SSIM curve in Fig.15. Fig.14 and Fig.15 illustrated that both the PSNR and SSIM curves have peaks, which reflect the existence of maximum image quality. The result clearly showed that the optimal tilt angle is different in two simulations. In the first simulation, the PSNR and SSIM curves are plotted by the red lines. The quality of reconstructed layer image is optimal at tilt angle around 80°, although the trend of the PSNR and SSIM curves are not identical. The tilt angle of maximum PSNR and SSIM is close to result of theoretical modeling. The curves drop sharply when approaching 90°. That phenomenon is also confirmed by theoretical predictions.

Same as the first simulation, the PSNR and SSIM curves of 254th layer image and 257th layer image at each sampling tilt angle are plotted by the blue lines in Fig.14 and Fig.15. The tilt angle of peak PSNR and SSIM curves is around 85° according to the figures, which is close to result of theoretical modeling. It is ascertained that the optimal tilt angle approaches 90° as the ratio $\frac{h_0}{r_0}$ increases infinitely. On the premise of parallel beam projections, CT scanning (when tilt angle $\varphi = 90°$) is more suitable for 'rod-shaped' objects rather than flat objects. However, in any case when the tilt angle is slightly less than 90°, it does help to improve the quality of reconstruction.

Based on the indicators above, we further obtained the optimal laminographic tilt angles of different $\frac{h_0}{r_0}$ ratios, as $\frac{h_0}{r_0} = \left(\frac{1}{80}, \frac{1}{20}, \frac{1}{3}, 1, 2, 4, 6\right)$. The line graph is shown in Fig.16, where the interval of tested tilt angles is 1°.

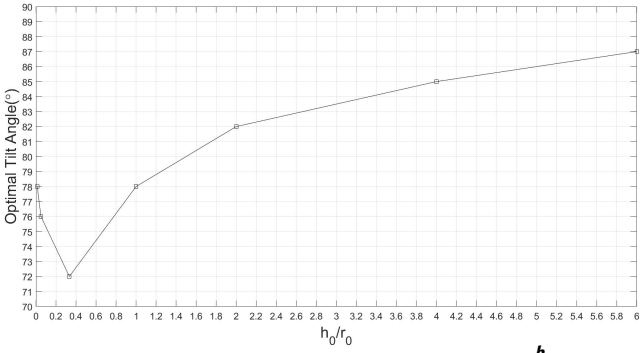

FIGURE 16. The experimental optimal tilt angles of different $\frac{h_0}{r_0}$ ratios of simulated cylindrical objects.

The proposed method provides a theoretical basis for obtaining the optimal scanning tilt angle. Compared with conclusions only through conventional simulations and experiments, the result acquired by this method is more suitable for objects with various shapes [13], [23]. Three indicators have been used to evaluate the image quality. Similar curves can be obtained by using other indicators [23].

VI. CONCLUSION

This article has briefly introduced the computed laminography as a superior method for imaging internal structures of flat objects. As a scanning geometric parameter, the laminographic tilt angle highly affect the quality of reconstruction. A method has been proposed to calculate optimal laminographic tilt angle. The method involves the two essential factors: the quantity information acquired by projections, the reconstructive solution domain of the object. We have evaluated the quantity information by measuring the entropy reduction caused by projection conditional constraints, and calculated the general volume of solution domain for regular shaped objects (cylindrical models). The optimization is about balancing the two factors, which adjusts the laminographic tilt angle for maximum ratio of the quantity information and the volume of solution domain. At last, a CL imaging simulation of cylindrical models was designed to verify the effectiveness of the method. The calculated theoretical optimal tilt angle was proved to be quite close to the experimental result. Meanwhile, the method is expected to be effective for other kinds of objects with clear boundaries, which requires more experiments.

REFERENCES

[1] P. C. Seynaeve and J. I. Broos, "The history of tomography," *Journal Belge De Radiologie*, vol. 78, no. 5, pp. 284–288, 1995.
[2] A. E. Buzzi and M. V. Suárez, "Tomografía lineal: Nacimiento, gloria y ocaso de un método," *Revista Argentina de Radiología*, vol. 77, no. 3, pp. 236–244, 2013.
[3] E. R. Miller, E. M. MoCurry, and B. Hruska, "An infinite number of laminagrams from a finite number of radiographs," *Radiology*, vol. 98, no. 2, pp. 249–255, Feb. 1971.
[4] M. D. Barker, "Laminographic reconstruction from real-time radiographic images," in *Review of Progress in Quantitative Nondestructive Evaluation*. Boston, MA, USA: Springer, 1989, pp. 457–464.
[5] B. D. Sawicka, "Computed laminography, limited-view tomography and fully 3-D image reconstruction," in *Proc. Symp. Appl. Math.*, vol. 3, 1995, pp. 70–74.

[6] J. Zhou, M. Maisl, H. Reiter, and W. Arnold, "Computed laminography for materials testing," *Appl. Phys. Lett.*, vol. 68, no. 24, pp. 3500–3502, Jun. 1996.
[7] S. Gondrom, J. Zhou, M. Maisl, H. Reiter, M. Kröning, and W. Arnold, "X-ray computed laminography: An approach of computed tomography for applications with limited access," *Nucl. Eng. Des.*, vol. 190, nos. 1–2, pp. 141–147, Jun. 1999.
[8] M. Ming and L. Zheng, "Study on limited projections in micro-focus X-ray swing laminography," in *Proc. Int. Conf. Comput. High Energy Nuclear Phys.*, 2001, pp. 4–006.
[9] L. Helfen, T. Baumbach, P. Mikulík, D. Kiel, P. Pernot, P. Cloetens, and J. Baruchel, "High-resolution three-dimensional imaging of flat objects by synchrotron-radiation computed laminography," *Appl. Phys. Lett.*, vol. 86, no. 7, 2005, Art. no. 071915.
[10] F. Xu, L. Helfen, A. J. Moffat, G. Johnson, I. Sinclair, and T. Baumbach, "Synchrotron radiation computed laminography for polymer composite failure studies," *J. Synchrotron Radiat.*, vol. 17, no. 2, pp. 222–226, Mar. 2010.
[11] L. Helfen, A. Myagotin, P. Mikulík, P. Pernot, A. Voropaev, M. Elyyan, M. Di Michiel, J. Baruchel, and T. Baumbach, "On the implementation of computed laminography using synchrotron radiation," *Rev. Sci. Instrum.*, vol. 82, no. 6, Jun. 2011, Art. no. 063702.
[12] F. Xu, L. Helfen, T. Baumbach, and H. Suhonen, "Comparison of image quality in computed laminography and tomography," *Opt. Express*, vol. 20, no. 2, p. 794, Jan. 2012.
[13] M. Rehak, U. Hassler, and R. Hanke, "Acquisition trajectories for X-ray tomosynthesis applied to planar samples," in *Proc. 2nd Int. Symp. NDT Aerosp.*, vol. 22, 2010, p. 24.
[14] J. Radon, "On the determination of functions from their integral values along certain manifolds," *IEEE Trans. Med. Imag.*, vol. MI-5, no. 4, pp. 170–176, Dec. 1986.
[15] Y. Geng, J. Tan, and C. Guo, "Computational coherentimaging by rotating a cylindrical lens," *Opt. Express*, vol. 26, no. 17, pp. 22110–22122, 2018.
[16] E. E. Daub, "Probability and thermodynamics: the reduction of the second law," *Isis*, vol. 60, no. 3, pp. 318–330, Oct. 1969.
[17] W. Feller, "A direct proof of Stirling's formula," *Amer. Math. Monthly*, vol. 74, no. 10, p. 1223, Dec. 1967.
[18] J. Fu, T. Biernath, M. Willner, M. Amberger, J. Meiser, D. Kunka, J. Mohr, J. Herzen, M. Bech, and F. Pfeiffer, "Cone-beam differential phase-contrast laminography with X-ray tube source," *EPL (Europhys. Lett.)*, vol. 106, no. 6, Jun. 2014, Art. no. 68002.
[19] Y.-H. Shiao, T.-J. Chen, K.-S. Chuang, C.-H. Lin, and C.-C. Chuang, "Quality of compressed medical images," *J. Digit. Imag.*, vol. 20, no. 2, p. 149, 2007.
[20] S. E. Ghrare, M. A. M. Ali, and M. Ismail, "The effect of image data compression on the clinical information quality of compressed computed tomography images for teleradiology applications," *Eur. J. Sci. Res.*, vol. 23, no. 1, pp. 6–12, 2008.
[21] R. M. S. Joemai and J. Geleijns, "Assessment of structural similarity in CT using filtered backprojection and iterative reconstruction: A phantom study with 3D printed lung vessels," *Brit. J. Radiol.*, vol. 90, no. 1079, Nov. 2017, Art. no. 20160519.
[22] M. Buty, Z. Xu, and A. Wu, "Quantitative image quality comparison of reduced-and standard-dose dual-energy multiphase chest, abdomen, and pelvis CT," *Tomography*, vol. 3, no. 2, p. 114, 2017.
[23] L. Yenumula, U. Kumar, and A. Dash, "X-ray industrial computed laminography (ICL) simulation study of planar objects: Optimization of laminographic angle," in *Industrial Tomography and Instrumentation Section, Isotope Production and Applications Division*. Mumbai, India: Bhabha Atomic Research Centre, 2015.

YIMING JIANG received the B.S. degree in measurement and control technology and instrument from the East China University of Science and Technology, Shanghai, China, in 2012. He is currently pursuing the Ph.D. degree (successive postgraduate and doctoral programs) in instrument science and technology with Tianjin University, Tianjin, China.

JING ZOU received the M.S. and Ph.D. degrees in applied mathematics from Capital Normal University, Beijing, China, in 2006 and 2009, respectively.

She is currently an Associate Professor with the School of Precision Instruments and Optoelectronics Engineering, Tianjin University, Tianjin, China. Her current research interests include x-ray imaging, image processing, and applied mathematics.

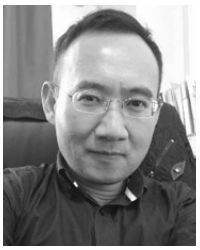

XIAODONG HU received the Ph.D. degree in measurement technology and instruments from Tianjin University, in 2000.

He has been involved in the research work of scanning probe testing and processing technology, micro optical testing theory and technology, as well as the independent research and development of frontier scientific instruments. He is responsible for more than ten national scientific research projects, such as the National Key Scientific Instrument and Equipment Development Project, the National High-tech Research and Development Program of China (863 Program), the National Program on Key Basic Research Project (973 Program), and the National Natural Fund Project. He has published more than 100 articles (included in SCI and EI), and over 20 patents for inventions. He also won the National Science and Technology Progress Award (second class): Research and Development of Downhole Tooling Detection Technology and Testing Platform, in 2005.

ZHENYE HAN, photograph and biography not available at the time of publication.

YANTAO MU, photograph and biography not available at the time of publication.

MING CHEN, photograph and biography not available at the time of publication.

YING XU received the Ph.D. degree in precision engineering from the University of Warwick. He is currently the Chairman of Tianjin Sanying Precision Instruments Company, Ltd.

He is also the British Chartered Engineer (CEng), a member of the Institution of Mechanical Engineers (MIMechE), a Senior Engineer, and also a Professor. He is the candidate of "The Recruitment Program of Global Experts" (Entrepreneurial Class), and also a National Major Scientific Instruments Special Project Leader in "The Twelfth Five-Year Plan." He has nearly 20 years of experience in the development of ultraprecision motion control new technology and new products and rich experience in project management and enterprise management. He is well versed in the precision motion positioning and measurement technology of nanometer and sub-nanometer range. He masters modern micro-technology (including X-ray microscopy imaging technology) and product development and application, is one of the international micro/nano test technology and equipment as well as ultraprecision motion control technology leaders. Nano-displacement platform, X-ray three-dimensional microscope, the full-diameter core scanner, and other products, are developed by his technical team, filling the blank of technology in domestic, and the technical indicators reaching the international advanced level.